A Lattice Boltzmann - Immersed Boundary method to simulate the fluid interaction with moving and slender flexible objects

Julien Favier[a,*], Alistair Revell[b], Alfredo Pinelli[c]

[a] *Laboratoire de Mécanique, Modélisation et Procédés Propres (M2P2) - CNRS UMR 7340 - Aix Marseille Université, Marseille, France.*
[b] *School of Mechanical, Aerospace and Civil Engineering (MACE), University of Manchester, United Kingdom.*
[c] *School of Engineering and Mathematical Sciences, City University, London, United Kingdom.*

Abstract

A numerical approach based on the Lattice Boltzmann and Immersed Boundary methods is proposed to tackle the problem of the interaction of moving and/or deformable slender solids with an incompressible fluid flow. The method makes use of a Cartesian uniform lattice that encompasses both the fluid and the solid domains. The deforming/moving elements are tracked through a series of Lagrangian markers that are embedded in the computational domain. Differently from classical projection methods applied to advance in time the incompressible Navier-Stokes equations, the baseline Lattice Boltzmann fluid solver is free from pressure corrector step, which is known to affect the accuracy of the boundary conditions. Also, in contrast to other immersed boundary methods proposed in the literature, the proposed algorithm does not require the introduction of any empirical parameter. In the case of rigid bodies, the position of the markers delimiting the surface of an object is updated by tracking both the position of the center of mass of the object and its rotation using Newton's Laws and the conservation of angular momentum. The dynamics of a flexible slender structure is determined as a function of the forces exerted by the fluid, its flexural rigidity and the tension necessary to enforce the filament inextensibility. For both rigid and deformable bodies, the instantaneous no-slip and impermeability conditions on the solid boundary are imposed via external and localized body forces which are consistently introduced into the Lattice Boltzmann equation. The validation test-cases for rigid bodies include the case of an impulsively started plate and the sedimentation of particles under gravity in a fluid initially at rest. For the case of deformable slender structures we consider the beating of both a single filament and a pair filaments induced by the interaction with an incoming uniformly streaming flow.

Keywords: Immersed Boundary, Lattice Boltzmann, flexible structure, flapping filaments, inextensibility, particle sedimentation

1. Introduction

Studying the dynamics of a slender body deforming and moving in an ambient fluid flow is an exciting research topic whose interest is growing in various scientific communities, as it is

*Corresponding author
Email address: Julien.Favier@univ-amu.fr (Julien Favier)

intrinsically interdisciplinary (structural mechanics, fluid mechanics, applied mathematics), and covers a broad range of applications (aeronautics, civil engineering, biological flows, paper industry etc.). Recently, this topic has been the focus of several comprehensive reviews (Païdoussis, 2004; Shelley and Zhang, 2011) which cover an abundant literature, spanning early theoretical considerations on the flag instability problem by Rayleigh (1878) to linear stability studies (Eloy et al., 2007) and experiments on beating filaments (Zhang et al., 2000; Eloy et al., 2008). Among the experimental studies undertaken, those conducted using soap films (Zhang et al., 2000; Zhu and Peskin, 2000) are of particular note as they can be considered to be a reasonable approximation of 2D fluid structure interaction scenarios; which is also the case of the numerical approach employed in the present study.

Indeed, the primary objective of this work is to propose a numerical framework capable of solving the fluid-structure interaction (FSI) problem; coupling in time and space the dynamics of a moving object (rigid or flexible) with the dynamics of the surrounding fluid. The culmination of this study is the simulation of flexible filaments interacting with a streaming flow (i.e., a one dimensional flapping flag), and a step-by-step validation of increasing complexity is undertaken to this end:

- We first consider moving rigid objects with prescribed motion, via the case of the impulsively started flat plate, to evaluate the numerical order of the method and assess sensitivity of the solver to tip singularities.
- We then consider cases of rigid objects falling under gravity, so as to examine the sensitivity to the computation of ε, a parameter unique to the current method, which provides a robust definition for the finite thickness of structures in FSI problems.
- Finally we construct a framework for flexible beating filaments and after testing the structural model in the absence of fluid, we proceed to investigate the coupled solver for both single and tandem filaments.

The beating filament case is a reference configuration, well documented for fluid structure interaction problems and provides an excellent test case for the proposed numerical methodology. Embedded in this deceptively simple problem are many of the principal ingredients of fluid structure interactions: large deformations, slender flexible bodies, inextensibility and the dynamic balance between bending and fluid forces. In the development of a robust structural model of a flexible filament it is necessary to consider tension, gravity, fluid force and the flexural rigidity; this last term accounts for the resilience of the structure to bending. As pointed out by Eloy et al. (2008) the rigidity plays an important role in the stability of the coupled system, as it counteracts the destabilizing effects of the local pressure drops induced by fluid unsteadiness. The bending terms take the typical form of a 4th derivative with respect to the curvilinear coordinate of the structure (Huang et al., 2007), and tension forces are determined in order to satisfy the imposed inextensibility of the structure. Limiting the structure's length prohibits stretching motions that would dissipate energy, and thus the total energy of the system is determined by the balance between bending forces and fluid forces.

So far, various numerical methods have been suggested in the literature to model the fluid flow in the context of *fluid flag* type interaction problems. A few examples are the work of Huang et al. (2007) using the immersed boundary method, Alben and Shelley (2008) dealing with inviscid flows, and that of Zhu and Peskin (2002) for viscous flows. To enforce the presence of the solid, as seen by the fluid, we resort here to a variant of the immersed boundary method originally

introduced by Zhu and Peskin (2002). This method is efficient, accurate and computationally cheap as demonstrated by a growing number of contributions on the subject appearing in the last two decades (Peskin, 2002). However, a problematic feature of almost all immersed boundary implementations based on finite-differences/volumes solvers for incompressible unsteady flows is the need for a pressure-correction step.

The fractional step treatment of the momentum equations is well known to deteriorate the accuracy of the solution at the immersed solid boundaries. Indeed, the pressure correction projection is typically performed after the use of the immersed boundary step which takes place within the predictive momentum stage. This has the additional weakness of removing a direct control on the corrected divergence-free velocity at the boundaries, thus systematically introducing a first-order error in time on the actual boundary values (Domenichini, 2008). The Poisson problem, solved to compute the value of the projector term (i.e., pressure or pressure correction), should incorporate Neumann type conditions on the immersed boundary. Their direct imposition in the linear system (Ikeno and Kajishima, 2007) turns out to be quite complicated and also affects the the matrix structure, thus inhibiting *de facto* the use of fast Poisson solvers. To overcome this problem Taira and Colonius (2007) suggested the use of Lagrangian multipliers associated to boundary values to impose the velocity boundary condition on the immersed solid. Those Lagrangian multipliers are then obtained by solving a system arising from an algebraic splitting of the full spatial operator of the Navier Stokes equations.

In the present work we consider a viscous incompressible flow modelled through the Lattice Boltzmann method, which directly provides the velocity field without any pressure-correction step. This feature allows for a direct imposition of the boundary conditions on the solid. Aside from this algorithmical advantage, the Lattice Boltzmann approach is also very attractive in the context of fluid-structure interactions as it is, by nature, suitable for micro-scale flows (bio-engineering applications are a typical example). Additionally, the method is intrinsically highly parallel thanks to the local nature of the computational algorithm. The coupling of immersed boundary method with lattice Boltzmann method was first introduced by Feng and Michaelides (2004), later on followed by several studies such as Wu and Shu (2009, 2010) who improved the baseline formulation, and Tian et al. (2011) who coupled the immersed boundary method to a multiblock Lattice Boltzmann method. In our formulation, we use an Immersed Boundary formulation based on the one introduced by Uhlmann (2005) and later on improved by Pinelli et al. (2010), originally developed for finite differences methods, which directly provides the force distribution exerted by the fluid on the structure without the introduction of any empirical parameter. With respect to this last point, as it will be detailed later, our method differs from the method of Zhu and Peskin (2002) since no empirical system of springs and dampers is introduced. Our formulation is similar in spirit to the comprehensive approach proposed by Huang et al. (2007) and the formulation later on presented in Wu and Shu (2009, 2010). However, it will be shown that the present methodology enables a precise definition for the hydrodynamic thickness of the filament in the formulation of the forces exerted by the fluid on the solid; an issue that has remained elusive in previous studies.

The paper is organized as follows. After the Introduction, Section 2 describes the way that the forcing terms are computed to impose the desired boundary values on the immersed objects and a brief summary of the forced Lattice Boltzmann method. The two following sections are dedicated to the modelling and numerical formulation of the interaction between a fluid flow and moving rigid bodies (Section 3) and flexible filaments (Section 4) with emphasis on the inextensibility condition and its relationship with the immersed boundary method. Finally, some conclusions and future perspectives will be drawn.

2. Mathematical formulation of the coupled Lattice Boltzmann-Immersed Boundary method

This section describes the global formulation employed to simulate the coupled dynamics of a moving object (rigid or flexible) interacting with a fluid flow using an Lattice Boltzmann-Immersed Boundary method.

2.1. Immersed boundary

We use the Immersed Boundary formulation developed by Pinelli et al. (2010) in the context of finite difference methods for the incompressible Navier Stokes equations. In this approach, as in several others (Fadlun et al., 2000; Feng and Michaelides, 2004), the fluid is discretized on a regular Cartesian lattice while the moving objects are discretized by a set of markers, evenly distributed on the solid surfaces that in general do not correspond with the lattice nodes where the fluid flow is described. The basic idea of the method consists of determining a body force distribution $\mathbf{f_{ib}}$ that restores the desired velocity boundary values on the immersed surfaces at each time step. In particular, each time advance is split in two stages: in the first, values of fluid momentum are advanced to the next time level without accounting for any immersed object. In the second, the requisite force distribution is determined from the updated momentum field, and applied in a corrector stage to ensure the proper values on the immersed boundary. Similarly to the algorithm proposed in Wu and Shu (2009), the restoring force is thus considered as unknown, and is determined in such a way that the non-slip boundary condition is enforced correctly. The key point of the procedure is related to the interchange of information between fluid and solid, discretized at different locations. Before providing further details on the transfer of information between the lattice and the markers, we will briefly review the basic idea behind the method.

Consider that we have obtained a macroscopic velocity field $\mathbf{u^p}$ obtained from the Lattice Boltzmann equations (see Equations 14-19 introduced further down), having advanced one time step without the introduction of any body force. Let $\mathcal{I}[\mathbf{u^p}](\mathbf{X}_k)$ be the value of the predicted velocity field interpolated at the k^{th} Lagrangian marker location $\mathbf{X}_k$ (from now on capital letters refer to variables evaluated at the Lagrangian markers, whilst lower case are used for the ones defined on the lattice nodes). We thus introduce a system of singular forces defined on the markers as:

$$\mathbf{F_{ib}}(\mathbf{X}_k) = \frac{\mathbf{U^{d}}^{n+1}(\mathbf{X}_k) - \mathcal{I}[\mathbf{u^p}](\mathbf{X_k})}{\Delta t} \tag{1}$$

Here, $\mathbf{U^{d}}^{n+1}$ denotes the target velocity value at the location $\mathbf{X}_k$ to be obtained at time step completion. It is computed based on the motion equations of the structure, forced by the fluid stresses (equation 22 for the case of rigid particles or equation 29 for the case of flexible slender bodies). It can be seen from Equation 1 that $\mathbf{F_{ib}}$ will enforce the desired value on the markers in a standard Navier Stokes time step. Loosely speaking, if *rhs* includes the sum of the advection, pressure gradient and viscous contributions (eventually taken at different time levels, depending on the time scheme) on the Eulerian grid, one would have:

$$\frac{\mathbf{U}^{n+1}}{\Delta t} = \frac{\mathbf{U}^{n}}{\Delta t} + \mathcal{I}[rhs] + \mathbf{F_{ib}} \tag{2}$$

Thus, Equation 2 leads to the equality $\mathbf{U}^{n+1} = \mathbf{U^{d}}^{n+1}$ on the markers since $\mathbf{U}^n/\Delta t + \mathcal{I}[rhs] = \mathcal{I}[\mathbf{u^p}]/\Delta t$. Neglecting truncation errors, the same reasoning holds true if the predicted field is estimated using the Lattice Bolzmann formulation 14-19 without the introduction of body forces.

Equation 2, as its lattice counterpart, is defined on the immersed boundary and therefore a further step is needed to carry out the same procedure on the fluid grid. To achieve a volumetric formulation of the immersed forces, we introduce a formal convolution with a Diracs delta comb $\delta(\mathbf{s})$ defined on the immersed boundary as

$$\mathbf{f_{ib}}(\mathbf{x}, t^{n+1}) = \frac{1}{\Delta t} \int_{\Gamma} \Big(\mathbf{U^d}(\mathbf{s}, t^{n+1}) - \mathcal{I}[\mathbf{u^p}](\mathbf{s}) \Big) \delta(\mathbf{x} - \mathbf{s}) d\mathbf{s}. \tag{3}$$

In Equation 3, s is a parametric coordinate defined along Γ. The value of the predicted macroscopic velocity field can be interpolated on to the immersed surfaces via convolution with a set of Diracs functions centered along Γ. Following Equation 3, the expression of the immersed force $\mathbf{f_{ib}}$ defined on the computational domain Ω that restores the desired conditions on the immersed boundary becomes:

$$\mathbf{f_{ib}}(\mathbf{x}, t^{n+1}) = \frac{1}{\Delta t} \int_{\Gamma} \left(\mathbf{U^d}(\mathbf{s}, t^{n+1}) - \int_{\Omega} \mathbf{u^p}(\mathbf{y}) \tilde{\delta}(\mathbf{y} - \mathbf{s}) d\mathbf{y} \right) \tilde{\delta}(\mathbf{x} - \mathbf{s}) d\mathbf{s} \tag{4}$$

where $\tilde{\delta}$ is a mollifier, to be defined later, that mimics the action of a Dirac's delta. In summary, the method requires a predictive step to obtain $\mathbf{u^p}$, a discrete convolution with a mollifier to obtain the singular force on Γ, another discrete convolution to determine the macroscopic body forces that restore the boundary values and a final step through Equations 14-19 to achieve the macroscopic velocity field at the next time level. It is worth mentioning that in the present time-stepping algorithm, in contrast with Peskin original method, no artificial parameter is introduced, for the price of computing a predicted field.

The mollifier $\tilde{\delta}$ that we have chosen to perform the convolution in Equations 3 and 4 is the one proposed by Roma et al. (1999):

$$\tilde{\delta}(r) = \begin{cases} \frac{1}{6}\left(5 - 3|r| - \sqrt{-3(1-|r|)^2 + 1}\right) & 0.5 \le |r| \le 1.5 \\ \frac{1}{3}\left(1 + \sqrt{-3r^2 + 1}\right) & |r| \le 0.5 \\ 0 & \text{otherwise} \end{cases} \tag{5}$$

where $r = x - s$ (the signed distance between any point $x \in \Omega$ and the position $s \in \Gamma$ where the mollifier is centered). The given function is indeed a mollifier since it is a continous function with compact support (i.e., $\tilde{\delta}(r) = 0$ for $|r| \ge 1.5$) and share with the Dirac's delta the properties:

$$i) \int_{-\infty}^{+\infty} \tilde{\delta}(x - s) dx = \int_{s-3/2}^{s+3/2} \tilde{\delta}(x - s) dr = 1; \; ii) \int_{-\infty}^{+\infty} (x - s)\, \tilde{\delta}(x - s) dr = \int_{s-3/2}^{s+3/2} (x - s)\, \tilde{\delta}(x - s) dr = 0 \tag{6}$$

If this convolution is used as an interpolator at s, these properties guarantee that the result is exact for both constant and linear functions. It is worth noting that more accurate interpolators may be introduced as necessary, via polynomial correction of the mollifier as in Pinelli et al. (2010). The multidimensional interpolator is built using a cartesian product (i.e., in 2D: $\tilde{\delta}(x, y) = \tilde{\delta}(x) \times \tilde{\delta}(y)$) while the discrete counterpart of the convolution integrals are simply built by using either a midpoint or a composite trapezoidal quadrature over a square in 2D (or a cube in 3D). The latter is centered on each Lagrangian marker with an edge of length 3 (supposing that the size of the lattice has been fixed to 1, as is convention). A sketch of the relationship between lattice, markers and supports is shown in Figure 1. The same mollifier used to interpolate the macroscopic velocity values from the uniform lattice to the immersed boundary nodes is also

used to perform the convolution that provides the body forces on the fluid lattice cells inside the support. In a 2D case, the discrete operator needed to carry out the integral along the immersed line Γ reads as:

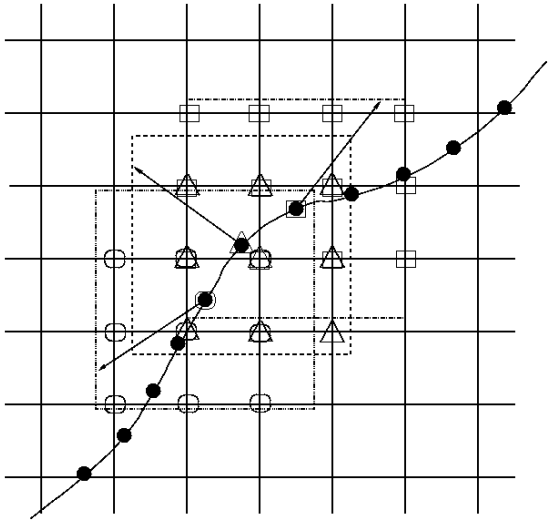

Figure 1: An immersed curve discretized with markers (•) and corresponding supports. Three consecutive markers are considered with the respective compact region and nodes: open symbols relate lattice node to a particular marker.

$$f_{ib}^{l}(x_i, y_j) = \sum_{n=1}^{N_e} F_{ib}^{l}(\mathbf{X_n})\tilde{\delta}(x_i - X_n, y_j - Y_n)\epsilon_n \tag{7}$$

where the superscript l refers to the l^{th} component of the immersed boundary force, (x_i, y_j) are the lattice nodes falling within the union of all the supports, N_e is the number of Lagrangian markers and ϵ_n are values to be determined to enforce consistency between interpolation and the convolution (i.e the force spread) as defined in 7. The discrete values ϵ_n can be physically interpreted as the local width of the strip $\epsilon(s)$ defined by the union of mollifiers distributed along the parametric coordinate of the immersed contour s. This geometrical interpretation allows one to define a hydrodynamic thickness of a one-dimensional filament in a clear and concise way. Crucially, the ϵ_n values are computed such that the interpolation and spreading operators are dual (Pinelli et al., 2010), as detailed below.

Consider any two dimensional smooth scalar function $g(x, y)$ interpolated on the markers located at $\mathbf{X}_i = (X_i, Y_i)$:

$$G(\mathbf{X}_i) = \sum_{k,l \in \mathcal{S}_i} g(\mathbf{x}_{l,k})\, \tilde{\delta}(x_{k,l} - X_i, y_{k,l} - Y_i)\, \omega_{k,l}, \quad i = 1, ..., N_e \tag{8}$$

where $\mathcal{S}_i$ is the set of lattice nodes falling within the support (3×3) of the ith marker and $\omega_{k,l}$ are quadrature weights. By replacing the values of $g_i(\mathbf{x}_{l,k})$ with those that would be obtained from the discrete spread (i.e. the convolution 7), the following conditions are obtained:

$$G(\mathbf{X}_i) = \sum_{k=1}^{N_e} a_{i,k}\, \epsilon_k\, G(\mathbf{X}_k), \quad i = 1, ..., N_e \tag{9}$$

In Equation 9, $a_{i,k}$ is the (discrete) integral of the product of the i^{th} and k^{th} mollifiers (centered at $\mathbf{X}_i$ and $\mathbf{X}_k$, respectively) over the support of the former multiplied by Δs (i.e., the spacings between markers along the immersed curve):

$$a_{i,k} = \Delta s \sum_{k,l \in \mathcal{S}_i} \tilde{\delta}(\mathbf{x}_{k,l} - \mathbf{X}_i)\, \tilde{\delta}(\mathbf{x}_{k,l} - \mathbf{X}_k)\, \omega_{k,l} \tag{10}$$

In matrix notation, and imposing that the relationships must hold for any function $g(x, y)$, the linear system 9 can be written as:

$$\mathsf{A}\,\vec{\varepsilon} = \vec{1} \tag{11}$$

with $\vec{1} = (1, 1, \ldots, 1)^T$ and $\mathsf{A} = \{a_{i,j}\}_{i,j=1\cdots N_e}$ ($a_{i,j}$ as in 10). In view of the compact support of each mollifier, A is a banded matrix (typically pentadiagonal when the spacing between immersed nodes is chosen to be the same as the lattice spacing). More details about the solution of the linear system 11 and the conditioning of matrix A can be found in Pinelli et al. (2010).

2.2. Lattice Boltzmann method

As mentioned in the introduction, the Lattice Boltzmann method (LBM) is attractive when dealing with fluid-structure interaction problems tackled with the immersed boundary methods, since the imposition of boundary values does not suffer from errors originating from projection step. It is also particularly well suited for massively parallelised simulations, as the time-advancement is explicit and the computational stencil is local. LBM has been extensively used in literature in the past decades (see Chen and Doolen (1998); Succi (2001) for a complete overview) and is now regarded as a powerful and efficient alternative to the classical Navier-Stokes solvers (see the formal proof in Shan et al. (2006)), including applications to high Reynolds and high Mach numbers e.g. coupled to Large Eddy Simulation (Malaspinas and Sagaut, 2012) or aeroacoustics (Marié et al., 2009).

The Lattice Boltzmann equation governs the transport for the time rate of change of particle distribution functions f, which represents a meso-scale 'patch' of fluid (i.e., the probability of finding a particle in a certain location with a certain velocity). In contrast to Navier-Stokes equations, which are formulated in terms of macroscale variables (velocity, pressure, temperature), the Lattice Boltzmann method operates at a mesoscopic level via the distribution functions f, which are simply summed to obtain the macroscopic dynamics (see Equations 18 and 19 further down). The Navier-Stokes equations can be recovered exactly from the Lattice Boltzmann equation using the Chapman-Enskog multiscale expansion (Qian et al., 1992).

The Boltzmann transport equation for the distribution function $f = f(\mathbf{x}, \mathbf{e}, t)$ at a node x and time t with particle velocity vector $\mathbf{e}$ is given as follows:

$$\frac{\partial f}{\partial t} + \mathbf{e} \cdot \nabla_{\mathbf{x}} f + \mathbf{F} \cdot \nabla_{\mathbf{e}} f = \Omega_{12}, \tag{12}$$

where $\mathbf{x}$ are the spatial coordinates, $\mathbf{e}$ is the particle velocity and $\mathbf{F}$ accounts any external force; in the present work this force is the body force $\mathbf{f_{ib}}$ applied to the fluid. Clearly this last term is very important as it will be used to convey the information between the fluid and the

structure. The collision operator Ω_{12} is simplified using the Bhatnagar, Gross, and Krook (BGK) approach (Bhatnagar et al., 1954), where it is assumed that local particle distributions relax to an equilibrium state $f^{(eq)}$ in a single relaxation time τ:

$$\Omega_{12} = \frac{1}{\tau}\left(f^{(eq)} - f\right). \tag{13}$$

Following He and Luo (1997) the discrete form of Equation 12 is obtained via a Taylor series expansion leading to:

$$f_i\left(\mathbf{x} + \mathbf{e_i}\Delta t, t + \Delta t\right) - f_i\left(\mathbf{x}, t\right) = -\frac{\Delta t}{\tau}\left(f\left(\mathbf{x}, t\right) - f^{(eq)}\left(\mathbf{x}, t\right)\right) + \Delta t F_i \tag{14}$$

Conceptually, the LBM algorithm is decomposed into two stages, embedded in Equation 14: first, the collision of particles (first term of the r.h.s. of the equation) which controls the relaxation toward equilibrium, and secondly, the streaming of particles (l.h.s of the equation) which drives the data shifting between lattice cells.

This equation is solved on the lattice, a Cartesian and uniform mesh in our case. At each point on the lattice, each particle is assigned one of a finite number of discrete velocity values. In our case we use the D2Q9 model, which refers to two-dimensional and nine discrete velocities per lattice node (which corresponds to the directions east, west, north, south, center, and the 4 diagonal directions). In Equation 14 the subscript i refers to these discrete particle directions. As is convention, a normalization is used so that the spatial and temporal discretization of the lattice are set to unity, and thus the discrete velocities are defined as follows:

$$\mathbf{e_i} = c\begin{pmatrix} 0 & 1 & -1 & 0 & 0 & 1 & -1 & 1 & -1 & 0 \\ 0 & 0 & 0 & 1 & -1 & 1 & -1 & -1 & 1 & 0 \end{pmatrix} \quad (i = 0, 1, ..., 8) \tag{15}$$

where c is the lattice speed defined by $c = \Delta x/\Delta t = 1$ with the current normalization.

The equilibrium function $f^{(eq)}\left(\mathbf{x}, t\right)$ can be obtained by Taylor series expansion of the Maxwell-Boltzmann equilibrium distribution (Qian et al., 1992):

$$f_i^{(eq)} = \rho\omega_i\left[1 + \frac{\mathbf{e_i}\cdot\mathbf{u}}{c_s^2} + \frac{\left(\mathbf{e_i}\cdot\mathbf{u}\right)^2}{2c_s^4} - \frac{\mathbf{u}^2}{2c_s^2}\right] \tag{16}$$

In Equation 16, c_s is the speed of sound $c_s = 1/\sqrt{3}$ and the weight coefficients ω_i are $\omega_0 = 4/9$, $\omega_{1,2,3,4} = 1/9$ and $\omega_{5,6,7,8} = 1/36$, according to the current normalization. The macroscopic velocity $\mathbf{u}$ in Equation 16 must satisfy the requirement for low Mach number M, i.e. that $\mid \mathbf{u} \mid /c_s \approx M << 1$. This stands as the equivalent of the CFL number for classical Navier-Stokes solvers.

Here, it is noteworthy that the multi-scale expansion of Equation 14 neglecting terms of $O(\epsilon M^2)$ returns the Navier-Stokes equations to second order accuracy. In this case the kinematic viscosity is related to lattice scaling as $\nu = (\tau - 1/2)/3$. Thus, this relation links the Reynolds number to the relaxation time τ.

Concerning the discrete force distribution F_i needed to keep into account the body force $\mathbf{f_{ib}}$, here we use the formulation proposed by Guo et al. (2002):

$$F_i = \left(1 - \frac{1}{2\tau}\right)\omega_i\left[\frac{\mathbf{e_i} - \mathbf{u}}{c_s^2} + \frac{\mathbf{e_i}\cdot\mathbf{u}}{c_s^4}\mathbf{e_i}\right]\cdot\mathbf{f_{ib}} \tag{17}$$

Once Equation 14 has been advanced in time (explicitly), the macroscopic quantities (moments of the distribution function) are obtained directly as follows:

$$\rho = \sum_i f_i \tag{18}$$

$$\rho \mathbf{u} = \sum_i \mathbf{e_i} f_i + \frac{\Delta t}{2} \mathbf{F} \tag{19}$$

According to (Guo et al., 2002), Equations 17 to 19 allow to recover the forced Navier-Stokes equations with second-order accuracy, even for the case in which the body force is non-uniform in space and unsteady.

In summary, let us now recall the global algorithm used for the fluid structure interaction problem. As detailed in §2.1, the Lattice Boltzmann Equation 14 is first advanced in space and time with the external force set to zero ($F_i = 0$), corresponding to the fluid state without structure, which provides the distribution functions f needed to build a predictive velocity using Equation 19. This fluid velocity is then interpolated onto the Lagrangian markers, which allow us to derive the forcing required to impose the desired boundary condition at each Lagrangian marker using Equation 1, which provides for a kinematic compatibility between solid and fluid motion, i.e. zero relative velocity on the solid boundary. Around each marker, the forcing is then spread onto the lattice neighbours using Equation 3. It is then discretized on the lattice discrete directions using Equation 17 and added to the r.h.s. of the lattice Boltzmann equation (term F_i in Equation 14) to be advanced once again in space and time. Finally, the macroscopic quantities are computed by equation 19, which closes one time step of the solver.

3. Fluid-rigid solid interaction

In this section we present and validate the methodology to simulate numerically the fluid-structure interaction between a moving rigid object and a surrounding fluid. For each validation case the mathematical formulation is first introduced, followed by corresponding numerical simulations. The validation cases are presented in order of increasing complexity: an impulsively started flat plate, the sedimentation of first a single particle and then of two rigid particles.

3.1. Formulation

We consider the case of solid objects moving through a fluid initially at rest. In particular, the formulation for freely sedimenting particles is briefly summarised hereafter as it encompasses all the cases that will be presented. Thus, we consider rigid circular disks denoting the center of mass of each individual particle (e.g., the mth one) by $\xi^m = (\xi^m_x, \xi^m_y)$ and the angle of rotation by θ^m (with respect to the initial position). At each time step, each 2D disk, (viz the mth one), discretized with N^m boundary markers placed at a distance of Δs_m apart, will experience a resulting total force and a total torque due to fluid interaction defined respectively as:

$$\mathbf{F}^m_{fs} = -\rho_f \Delta s_m \sum_{l=1}^{N^m} \epsilon^l \mathbf{F}^l_{ib} \tag{20}$$

$$\mathbf{T}^m_{fs} = -\rho_f \Delta s_m \sum_{l=1}^{N^m} \epsilon^l (\mathbf{X}_l - \xi^m) \times \mathbf{F}^l_{ib} \tag{21}$$

According to Newtons laws, each particle accelerates as:

$$\ddot{\xi}^m = \frac{\mathbf{F}_{fs}}{(\rho_p^m - \rho_f)V_m} + \mathbf{g} \tag{22}$$

In the expression above, V_m refers to the volume of the particle (of radius R_m), ρ_f and ρ_p^m are respectively the densities of the fluid and of the mth particle, and $\mathbf{g}$ is the gravitational acceleration. Also, the rotational velocity of the particle can be computed using the conservation of the angular momentum:

$$\ddot{\theta}^m = \frac{\mathbf{T}_{fs}}{\rho_p^m V_m R_m^2/2} + \rho_f \frac{d}{dt}\int_{V_m} \mathbf{r}\times\mathbf{u}\, dv \tag{23}$$

The last term in Equation 23 represents the rate of change of angular momentum inside the solid domain and stems from the fact that, in general, the flow inside the solid domain does not exactly satisfy the rigid-body constraint if forcing is only applied along the circumference of the particle. The actual value of the rotational velocity $\dot{\theta}^m$ has no direct impact on the motion of the particle center of mass but it is used to determine the desired velocity on the particle boundary needed to compute the immersed boundary force (i.e. in Equation 2: $\mathbf{U}^{n+1}(\mathbf{X_k^m}) = \dot{\xi}^m + \dot{\theta}^m \times \mathbf{r}_k^m$, where $\mathbf{r}_k^m$ is the kth marker $\mathbf{X_k^m}$ in a reference frame mounted on the mth center of mass). The given equations of motion of the particles are advanced in time using a classical second-order leap frog scheme.

3.2. Impulsively started flat plate

The first validation case that we consider concerns the simple case of an infinitesimally thin finite flat plate of height h, suddenly accelerated from rest to a constant velocity U_0 in the direction normal to its surface in a fluid at rest. In this case, the dynamics of the flat plate are directly prescribed, leading to a one-way coupled problem, i.e. the velocity of the plate is not influenced by the surrounding flow. Despite being a simplification of the general scenario given in §3.1, this case is particularly useful for the purposes of validating our numerical approach. Indeed an accurate prediction of the flow is dependent on capturing the fluid vorticity shed from the moving sharp tips of the plate, as well as the capability to deal with a one-dimensional object that behaves as a strip of finite thickness. We compare our results with the simulations performed by Mittal et al. (2008), obtained by a direct-forcing method, and with the results of Koumoutsakos and Shiels (1996) who employed a vortex-particle method. The results obtained with our methodology are at a Reynolds number of $Re_h = U_0 h/\nu = 1000$, based on plate height. The size of the computational domain is 12h $\times$ 9h (in the streamwise and normal direction), discretized by a uniform Cartesian lattice of 800 $\times$ 500 points, while 60 equispaced markers are used to discretize the vertical plate (positioned so that $ds = dx$).

Figure 2a displays the evolution of the wake vorticity behind the plate at three instants in time (the plate is moved from right to left; the non-dimensional time tU_0/h is used for the comparison). The topology of the recirculating flow behind the plate is well recovered as compared to the reference results (Fig. 18 of Mittal et al. (2008) and Fig. 5 of Koumoutsakos and Shiels (1996)). Figure 2b presents the temporal variation of the predicted non-dimensional bubble length s/h, computed as the length of the reversed flow along the centerline behind the plate. Overall, the numerical method is observed to handle well the motion of extremely thin bodies and the singular points occurring at each end.

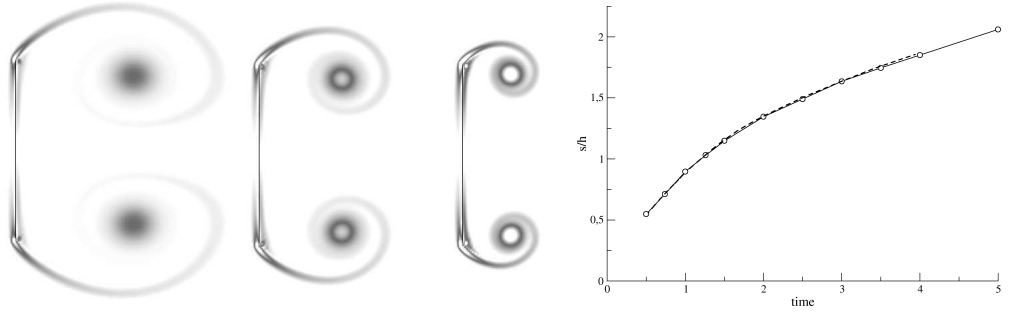

(a) (b)

Figure 2: (a): Three snapshots of vorticity contours obtained in the wake of an impulsively started flat plate (moving from right to left, $tU_0/h = 0.5$, $tU_0/h = 1$ and $tU_0/h = 2$). (b): Non-dimensional length s/h of the reversed-flow region behind the plate as a function of the non-dimensional time tU_0/h. Solid line and circles corresponds to the present results, Dashed lines are values obtained by Koumoutsakos and Shiels (1996).

A grid convergence analysis is also conducted on this case to assess the order of our numerical method. To this end, we assume the finest grid results as the reference. Keeping as constants both the Reynolds number and the ratio between number of lattice nodes and the number of markers on the plate for each simulation, we systematically coarsen the discretization of the plate from $n = 200$ down to $n = 25$. For each n, the L2 norm of the difference of the normal force on the plate (given by Equation 20) with the one obtained from the reference case is shown in Figure 3. A superlinear convergence is observed with a mean slope of about 1.4.

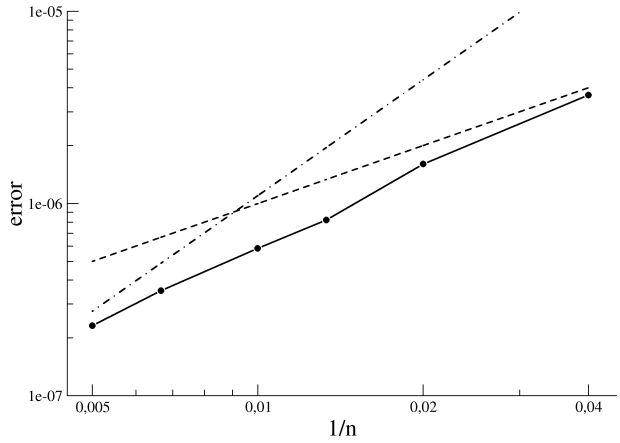

Figure 3: L2 norm of the error computed as a function of the grid refinement $1/n$. Dashed lines indicates convergence rates of order 1 and point-dashed line indicates order 2.

3.3. Sedimenting particles

Following the formulation presented in §3.1, we now consider particles sedimenting under the action of gravity in a fluid initially at rest. The primary motivation here is to explore the

sensitivity of the method to values of ε, so as to understand if recomputation of this quantity is required at each time step when dealing with rigid bodies that move with respect to the fixed lattice. In the event that this is not required, the entries in matrix **A** of Equation 11 can be approximated out of the computational loop with a high order composite Gaussian quadrature. With this technique, the obtained values of ε are found to be approximately constant: the values along the circle are independent of the relative position of the disk with respect to the lattice, within small local variations that weakly depend on the superposition of the supports. Motivated by this observation, we also perform simulations by fixing ε to a constant value computed analytically. Indeed, ε can be approximated using a constant value obtained by considering the continuous counterpart of equation 10 to fill in the elements of matrix A in equation 11, and then by taking the reciprocal of the average sum of the row elements (that turns out to be almost independent of the positions of the immersed markers when considering large diameters). While for fixed geometry no computational advantage is gained (since the ε distribution can be computed in a preprocess stage), in the case of moving objects this approximation leads to a substantial advantage that becomes more and more important as the number of immersed objects is increased. Both approaches for the computation of ε are compared hereafter.

A second motivation explored in this test case is to examine situations involving a direct particle-particle interaction. This occurs when both particles are in close proximity to each other, albeit so close that collision with film rupture can occur. In this circumstance, the thin layers of fluid remaining between particles cannot be resolved by grid sizes employed here, and therefore the establishment of a lubrication repulsive pressure cannot be properly captured. A direct consequence of this local under-resolution can lead to a partial overlap of the supports defining the boundaries of the interacting particles. To avoid this unphysical behaviour, we employ a localized repulsion force as the one described in Glowinski et al. (2001) with a force range of $3\Delta x$ to avoid supports overlap.

The first scenario studied here is the sedimentation of a single particle and the second one the sedimentation of two particles in a classical *drafting–kissing–thumbling* situation. In both cases a first-order 'bounceback' condition is applied at the domain edges of the lattice (i.e. the particles sediment in a closed channel). Table 1 summarises the numerical parameters used for the simulations.

	A1	B1	C1	D1	A2	B2	C2	D2
Particle no.	1	1	1	1	2	2	2	2
Diameter, D	150	150	200	200	140	140	200	200
ε	f: 1.86	d	f: 2.0	d	f: 1.86	d	f: 2.0	d
N_x	2850	2850	3800	3800	5050	5050	7214	7214
N_y	1470	1470	1950	1950	1250	1250	1784	1784

Table 1: Particles sedimentation test cases. Cases A1 $\cdots$ D1: single sedimenting particle. Cases A2 $\cdots$ D2: two sedimenting particles initially separated by 2 diameters along the gravity direction. In the ε row, f refers to a fixed value and d to a dynamically computed value of ε. N_x is the number of nodes in the gravity direction and N_y in the normal-to-gravity direction.

All cases share the same density ratio of the particle density over the fluid density $\rho_p/\rho_f = 1.5$, and the same non-dimensional G number given by

$$G = \frac{Re^2}{Fr} = \frac{D^3|\mathbf{g}|}{\nu^2} \tag{24}$$

Fr is the Froude number defined by $Fr = U^2/(|\mathbf{g}|D)$. As suggested by Aidun and Ding (2003), this non-dimensional parameter allows for the imposition of a dynamical similarity without the need for a characteristic velocity. In our case the value of $G = 1.53 \times 10^5$ matches the simulation of Uhlmann (2005) for both single and two particles sedimentation cases. Having fixed $\nu = 0.05$ and the particle diameter, the similarity is obtained by computing the gravity acceleration needed for G to take on the desired value. The Reynolds numbers based on the terminal velocity $Re = U_{max}D/\nu$ obtained for the single particle simulations are: (A1) 313.2; (B1) 307.8; (C1) 312.0 and (D1) 308.0, which are close to 329.8, obtained for the same by Uhlmann (2005).

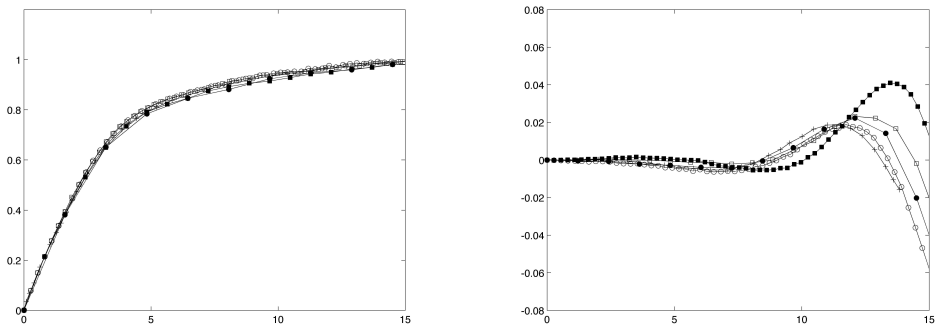

(a) u/U_{max} (parallel to gravity). (b) v/U_{max} (normal to gravity).

Figure 4: Non-dimensional particle velocity components versus non-dimensional time tU_{max}/D for the sedimentation of a single particle. Symbols: • case A1, ■ B1, ∘ C1, □ D1 and + Uhlmann.

In Figures 4a and 4b the time evolution of the velocity of a single sedimenting particle in cases A1 to D1 is compared with Uhlmann (2005). At a first glance, larger discrepancies for the v component appear as compared to the other velocity component u aligned with gravity, although the scale is considerably smaller for the former. Regardless, the normal to gravity velocity component presents low amplitude oscillations transverse to the motion that are much harder to reproduce. Nevertheless, we obtain a better comparison with Uhlmann (2005) results when increasing D. Indeed, increasing the diameter corresponds to an increase of the spatial resolution since we obtain a higher density of markers along the circle for the same particle Reynolds number. It is also noteworthy that results obtained with a dynamic computation of ε are better for the finer resolution than for the coarser resolution. For a resolved simulation, fixing the value of ε does not introduce any significant error (increasing the diameter decreases the curvature making the approximate value quite close to the real one). Globally, data comparison shows a good agreement with a quite low relative difference with respect to the reference results. Moreover, by increasing the grid node density our results at constant ε approach the reference data (also obtained with a fixed ε) by Uhlmann (2005).

We now present results concerning the sedimentation of two particles initially aligned with gravity, with an offset of two diameters between the particles centres (cases A2 to D2 in table 1). The dynamics are schematically illustrated in Figure 5, showing vorticity snapshots representative of the three classical stages. We perform the validation up until the *kissing* stage only, since afterwards the comparison is strongly sensitive to the intensity of the repulsive force

model; which comprises empirical quantities. Figure 6 presents a quantitative comparison between the results obtained in the cases C2 and D2 of Table 1 versus the reference data of Uhlmann (Uhlmann, 2005) in terms of particles velocity components.

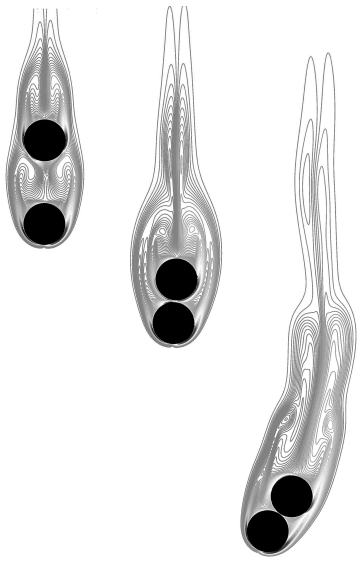

Figure 5: Sedimentation of two particles with gravity oriented from top to bottom showing the drafting (left), the kissing (center) and the thumbling (right) stages represented by snapshots of iso-vorticity obtained from the A2 case of table 1.

The present results demonstrate reasonably good agreement with the reference results, for what is undoubtedly a challenging configuration, involving two-way coupled dynamics and wake interactions. As expected, the major discrepancies are found on the velocity components after the direct interaction of the particles. Those discrepancies are explained by the intensity of the repulsive force in the transverse direction.

4. Fluid-flexible filament interaction

This section presents the interaction between flexible slender structures with an incoming fluid stream. After presenting the mathematical and numerical formulation of the problem, we consider the cases of a single flexible filament and of side-by-side two flexible filaments flapping in an incoming fluid flow under the influence of gravity.

4.1. Mathematical formulation

We consider a flexible filament-like structure of length L, linear density ρ_s, immersed in a fluid of density ρ_f and subject to a gravitational acceleration $\mathbf{g}$. As in §2.1, $\mathbf{X}$ refers to the Cartesian coordinates of the markers and $\mathbf{F}_{ib}$ the force exerted by the filament on the fluid (also defined on each marker). The latter is related to its lattice counterpart $\mathbf{f}_{ib}$ by:

$$\mathbf{F}_{ib}(\mathbf{X}) = \int_{\Omega} \mathbf{f}_{ib}(\mathbf{x})\tilde{\delta}(\mathbf{x} - \mathbf{X})dV \tag{25}$$

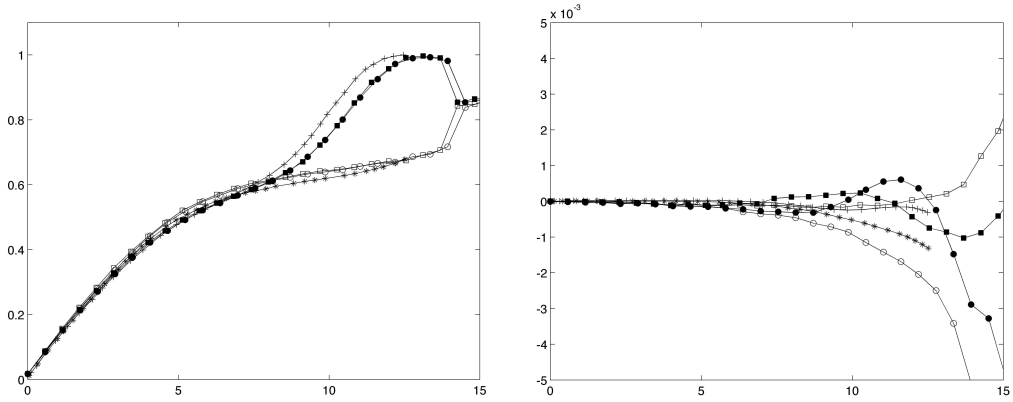

(a) u/U_{max} (parallel to gravity). (b) v/U_{max} (normal to gravity).

Figure 6: Non-dimensional particle velocity components versus non-dimensional time tU_{max}/D for the sedimentation of two particles. Symbols: • case C2 trailing particle, ∘ C2 leading particle, ■ D2 trailing particle, ▫ D2 leading particle, + Uhlmann trailing and ∗ leading particles, respectively.

where Ω represents a control volume and $\tilde{\delta}$ the mollifier defined in §2.1. From now on, the following notations will be used: E refers to the Young's modulus of the filament, I is the moment of inertia of the filament ($K_B = EI$ the flexural rigidity of the filament), and T the tension within the filament. The equations governing the motion of the filament in a time interval from $t = 0$ to t, can be obtained by seeking a stationary point of the action integral $J = \int_0^t \mathcal{L} dt$, where $\mathcal{L}$ is the Lagrangian, which in this specific framework takes on the following expression:

$$\mathcal{L} = \int_\Gamma \frac{\Delta\rho}{2}\left(\frac{d\mathbf{X}}{dt}\right)^2 ds - \int_\Gamma \left[\frac{EI}{2}\left(\frac{d^2\mathbf{X}}{ds^2}\right)^2 + \frac{T}{2}\left(\frac{d\mathbf{X}}{ds}\right)^2\right] ds + \int_\Gamma \Delta\rho \mathbf{g}\mathbf{X} ds - \int_\Omega \rho_f \mathbf{f}_{ib}\,\mathbf{X}\,\tilde{\delta}(\mathbf{x}-\mathbf{X})\, dV \quad (26)$$

In 26, the density difference $\Delta\rho = \rho_s - \rho_f L$ comes from the Archimedes' law and Γ stands for the range of integration along the filament. The four terms appearing in 26 represent, respectively: the kinetic energy, the elastic potential energy, the works done by the gravity and by fluid forces. Transforming the volume integral appearing in the fourth term of Equation 26 into a line integral by absorbing the $\tilde{\delta}$ term, we obtain the following expression for the action integral:

$$J = \int_0^t \int_\Gamma \left[\frac{1}{2}\Delta\rho\left(\frac{d\mathbf{X}}{dt}\right)^2 - \frac{1}{2}K_B\left(\frac{d^2\mathbf{X}}{ds^2}\right)^2 - \frac{1}{2}T\left(\frac{d\mathbf{X}}{ds}\right)^2 + \Delta\rho\mathbf{g}\mathbf{X} - \varepsilon\rho_f \mathbf{F}_{ib}\mathbf{X}\right] ds dt \quad (27)$$

It is noteworthy that translating the work done by the fluid forces from a surface integral to a line integral is only possible because we have an expression $\epsilon(s)$ for the hydrodynamic thickness of the filament given by Equation 7. This observation enables us to overcome the theoretical obstacle concerning the definition of the filament thickness reported by Huang et al. (2007), who instead adopted to the use of a non-rigorous, but physically sound, length scale. By vanishing the differential variation of J with respect to X and after successive partial integrations, the following equation governing the motion of the filament is found:

$$\Delta\rho\frac{d^2\mathbf{X}}{dt^2} = (T\mathbf{X}_s)_s - K_B\mathbf{X}_{ssss} + \Delta\rho\mathbf{g} - \varepsilon\rho_f\mathbf{F}_{ib} = 0 \tag{28}$$

The subscript s in Equation 28 denotes the spatial derivative along the parametric coordinate defined along the filament. A non-dimensional form of 28 can be obtained by multiplying by $L/(\Delta\rho U_\infty^2)$, U_∞ being the velocity of the incoming fluid. The reference quantities used for the non-dimensionalization are: the reference force tension $T_{ref} = \Delta\rho U_\infty^2$, the reference bending rigidity $K_{Bref} = \Delta\rho U_\infty^2 L^2$ and the reference Lagrangian forcing $F_{ref} = \frac{\Delta\rho}{\varepsilon\rho_f}U_\infty^2$. For convenience, from now on, the non-dimensional variables are written keeping the same notations as their dimensional counterparts:

$$\frac{d^2\mathbf{X}}{dt^2} = (T\mathbf{X}_s)_s - K_B\mathbf{X}_{ssss} + Ri\frac{\mathbf{g}}{g} - \mathbf{F}_{ib} \tag{29}$$

where the Richardson number is defined as $Ri = gL/U_\infty^2$. The resulting unknowns of the problem are, for each marker, the tension $T(s,t)$ and the filament spatial configuration determined by $X(s,t)$ and $Y(s,t)$. The closure of the equations is provided by the inextensibility condition that reads:

$$\mathbf{X}_s \cdot \mathbf{X}_s = 1 \tag{30}$$

This condition basically ensures that the filament does not stretch, and thus its length remains constant. The boundary conditions are $\mathbf{X} = \mathbf{X}_0$, $\mathbf{X}_{ss} = 0$ for the fixed end and $T = 0$, $\mathbf{X}_{ss} = 0$ for the free end. Equations 29 and 30 are discretized in a staggered fashion following Huang et al. (2007)'s formulation, by placing the tension point between coordinate markers, as shown in Figure 7 (left).

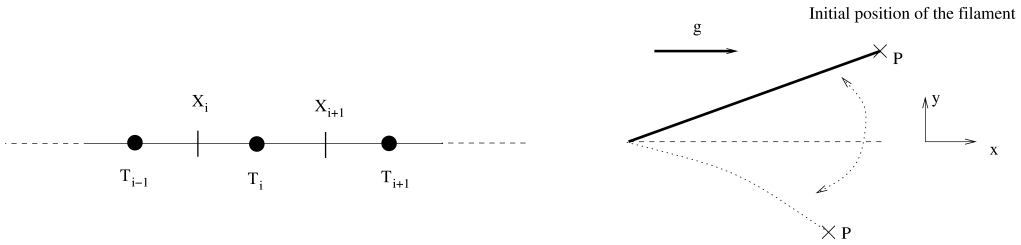

Figure 7: Left: Staggered discretization grid on the filament. Tension points are displayed as black circles, in between the coordinate markers. Right: Initial position of the filament falling under the action of gravity. The y-position of point P is monitored.

The set of discretized equations read:

$$\frac{\mathbf{X}^{n+1} - 2\mathbf{X}^n + \mathbf{X}^{n-1}}{\Delta t^2} = [D_s(T^{n+1}D_s\mathbf{X}^{n+1})] - K_B D_{ssss}\mathbf{X}^n + Ri\frac{\mathbf{g}}{g} - \mathbf{F}^n \tag{31}$$

$$D_s\mathbf{X}^{n+1} \cdot D_s\mathbf{X}^{n+1} = 1$$

where D_s refers to the standard second-order centered finite difference derivative approximation with respect to the parametric coordinate. At each time step, the resulting non-linear system

of equations is solved using a Newton method, by computing the exact Jacobian matrix which directly incorporates the given boundary values.

4.2. Filament model without fluid

To check the consistency of the numerical model of the filament, we first consider the case of a flexible filament oscillating and bending under the action of gravity (a pendulum) in absence of surrounding fluid. On this particular configuration, neglecting the bending term and in the limit of small angles, Huang et al. (2007) derived an analytical solution of Equation 29 without bending terms using a perturbation method (See appendix of Huang et al. (2007) for more details). To remain within the small angle approximation, we perform this test by setting the initial angle of the filament equal to $\theta_0 = 2^o$. Having fixed $K_B = 0$ and the gravity to a value equivalent to $Ri = 10$, we monitor the time evolution of the coordinate of the free extremity (point P on Figure 7). Figure 8a shows that the results obtained are in excellent agreement with the analytical solution (curves are stacked).

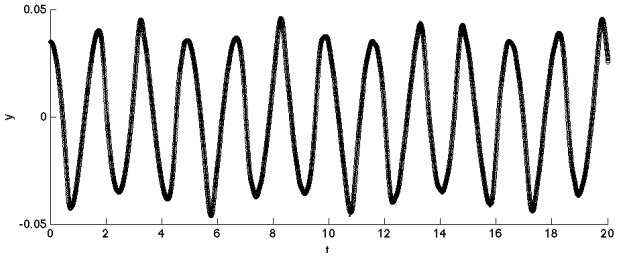

(a) $K_B = 0$ and $\theta_0 = 2^o$.

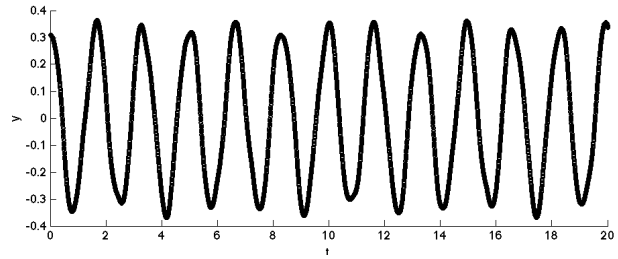

(b) $K_B = 0.01$ and $\theta_0 = 18^o$.

Figure 8: Time evolution of the y-coordinate of the free end without fluid (only gravity), without bending (top) and with bending (bottom). The present model is shown by circles, and is exactly stacked on reference results by the analytical solution under the small angles assumption (top) and by the numerical study of Huang et al. (2007) (bottom).

A second validation case for larger deflection angles (initial angle of $\theta_0 = 18^o$), is performed without fluid but including the bending terms ($K_B = 0.01$); results are displayed in Figure 8b. In comparison with the numerical results of Huang et al. (2007), a good agreement is obtained here also.

4.3. Flexible filaments beating in an incoming fluid flow

Here we focus on the dynamics of inextensible flapping filaments in a fluid flow. We start by considering the response, to gravity and hydrodynamics forces, of a single filament fixed at one

end. The mathematical framework presented in 4.1 is used with the tension computed to enforce filament inextensibility. We compare our results to the same set of experiments as those used by Zhu and Peskin (2002), and with the numerical results obtained by Huang et al. (2007). We fix the value of $\Delta\rho = 1.5$, the non-dimensional bending rigidity to $K_B = 0.001$, and the value of the Richardson number to $Ri = 0.5$. The non-dimensional inlet velocity is set to $U_\infty = 0.04$ (aligned with gravity direction), the relaxation time is $\tau = 0.524$ and the length of the filament is set to $L = 40$. These values lead to a Reynolds number $Re = U_\infty L/\nu$ equal to 200. The size of the computational domain is set to $10L \times 15L$, in the transverse and streamwise direction respectively. The lattice discretization (600×400 nodes) has been determined as the result of a preliminary grid convergence study. The initial angle of the filament is set to $\theta = 18^o$ with respect to the gravity direction, and its fixed end is placed at the centerline of the domain, at a distance of $4L$ from the inlet. The L2 norm of the inextensibility error is kept below 10^{-12} systemically at all times.

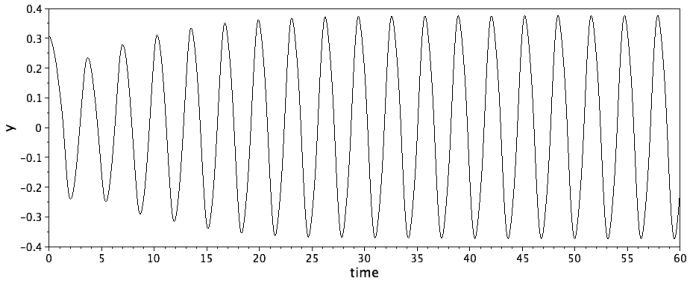

(a) y-coordinate of the free end.

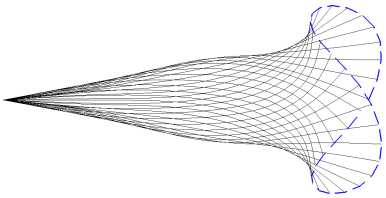

(c) Periodic flapping pattern.

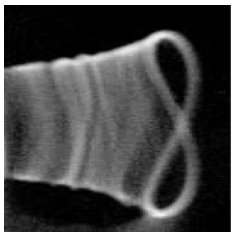

(d) Free end trajectory observed in Zhang et al. (2000).

Figure 9: Beating pattern of the single flapping filament immersed in fluid at $Re = 200$, $Ri = 0.5$, $\Delta\rho = 1.5$. (a): Periodic time evolution of the y-coordinate of the free end (in a uniform fluid flow going from left to right). The periodic motion over one flapping cycle obtained in the established state is shown in (b): using the present numerical framework (with $K_B = 0.001$) and in (c): from the experiments of Zhang et al. (2000).

Figure 9a displays the time evolution of the y-coordinate (transverse direction) of the free end of the filament. After six beating cycles, a periodic orbit is established with a period of 3 time units (the same as that indicated by Huang et al. (2007)). Also, the amplitude of the beating compares well: the difference with reference data on the maximal excursion of the free end is less than 5%. Figure 9b shows the periodic pattern of the beating in the established regime, characterised by sinuous traveling waves moving and amplifying downstream from the fixed end, as observed in Bagheri et al. (2012) as well as in the experiments of Shelley and Zhang (2011). In particular, the trajectory of the free end exhibits a characteristic *figure-eight* orbit (dashed line in 9b) similar to those reported in the soap film experiments used by Zhang et al. (2000) (Figure

9c), even though the latter experiments were obtained at a higher Reynolds number, of order 10^4.

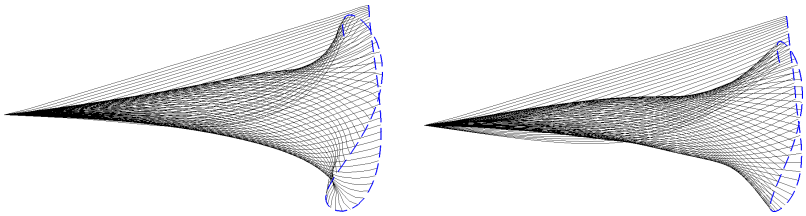

(a) Totally flexible filament ($K_B = 0$). (b) Rigid filament ($K_B = 0.001$).

Figure 10: Superimposed view of the instantaneous snapshots of the flapping filament without bending (a) and with bending (b) starting from an angle $\theta_0 = 18^o$. The trajectory of the free end is shown in dashed line.

Figures 10a and 10b illustrate the effect of the bending rigidity coefficient on the beating pattern. Without bending rigidity (Figure 10a), the filament is totally flexible and the free extremity is observed to 'roll up' at the point of maximum transverse displacement. This effect has been termed as *kick* after the works of Bailey (2000). On the other hand, when the filament has a finite flexural rigidity ($K_B = 0.001$ in this simulation), the rolling up of the free end is inhibited, thus the *kick* disappears and the flapping amplitude is reduced. Thus the proposed slender structure model, incorporating both bending terms and tension, to enforce inextensibility, is observed to reproduce the same phenomena as those observed experimentally.

Figure 11 provides a more detailed look at the time evolution of the vertical excursion of the free end, together with the instantaneous values of the works done by bending, tension and fluid forces (computed as in Equation 26).

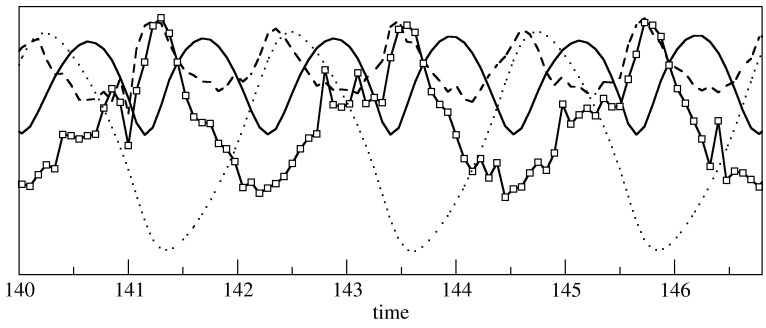

Figure 11: Time evolution of the energy balance between tension, bending and fluid forces. The various quantities are rescaled to appear on the same graph for the sake clarity. Solid line: Bending energy for $K_B = 0.001$; Dashed line: Tension; squares: Work exerted by the fluid on the filament for $K_B = 0.001$; Dotted line: y-coordinate of the free end

We note that the energy associated with bending systematically presents maximal values following the maximal values of the vertical displacement. On the other hand, the work done by the fluid forces reaches extrema that anticipate the maximal displacement. Thus, both contributions play a stabilizing role: fluid forces limit the maximal excursion of the filament, while later, bending operates to straighten the shape of the filament. Also, the behaviour of the tension during the three flapping cycles shown in the figure follows the same quasi-periodic evolution of

the bending action, as it also comes into play when the free end reaches an extremum. Thus, the combined action of flexural rigidity and tension of the filament tends to balance the global energy by decreasing the stresses exerted by the fluid on the filament. This *reaction* mechanism, which can be seen as a shape adaptation, is driven by the magnitude of the flexural rigidity. Decreasing it has the consequence of increasing the work done by the fluid forces, up to the limiting case of $K_B = 0$, where the *kick* is observed.

Next, we consider the scenario of two filaments flapping in a tandem configuration (side by side) comparing the different regimes that can be obtained by varying the distance between them d/L. In particular, we focus on the configurations experimentally studied by Zhang et al. (2000). The same non-dimensional values, the same domain size and the same initial angles ($\theta = 18^o$) are kept as in the case of the single beating filament.

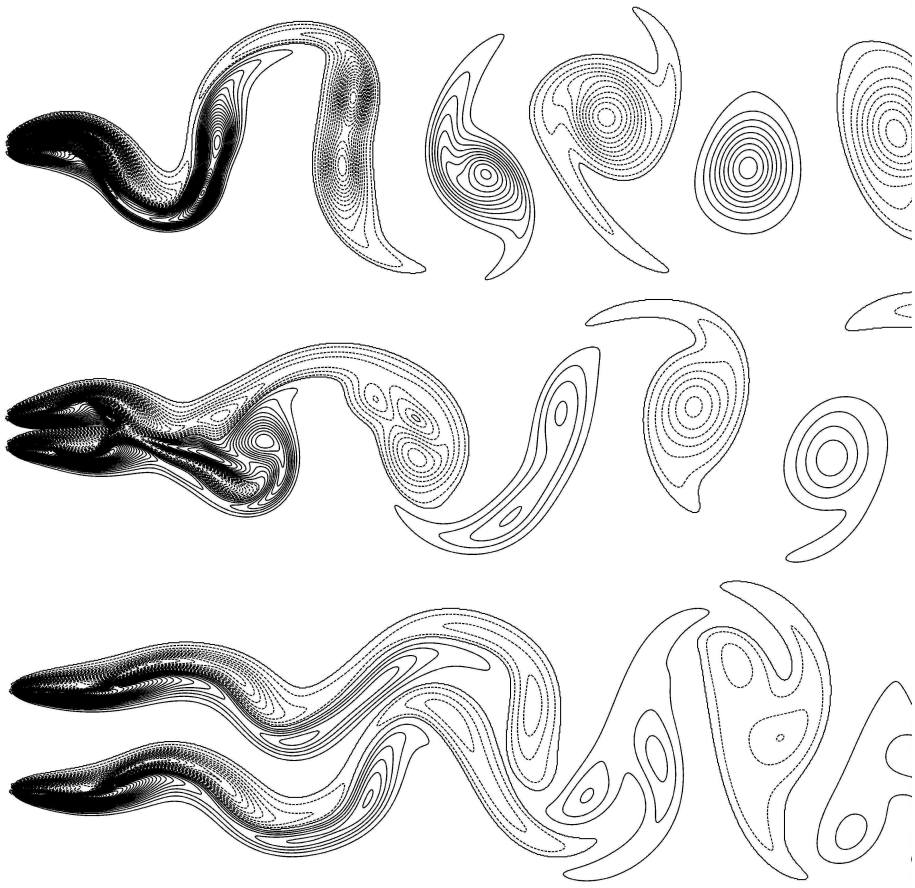

Figure 12: Snapshots of iso-vorticity for the case of two beating filaments using $\rho = 1.5$, $K_B = 0.001$, $Re = 300$, $Ri = 0.5$ and two different spacings. (a) $d/L = 0.1$, (b) $d/L = 0.3$, (c) $d/L = 1.0$.

Zhang et al. (2000) report that varying the spacing d/L leads to the appearance of different flow/filaments regimes. Their experiments reveal a symmetric flapping mode for distances

$d/L < 0.21$. For higher values, a bifurcation towards a regime characterised by an out-of-phase flapping mode is detected. Figure 12 displays the snapshots of iso-vorticity from the three different spacings. The wakes are characterised by a periodic vortex shedding and by a flapping motion of the filaments (shown in figure 13 for the three cases).

While the spacing is small ($d/L = 0.1$), the filaments remain very close to each other and behave almost as a single thick filament (see Figure 12a), resulting in an in-phase beating of the filaments, as displayed in Figure 13a. In contrast, when increasing the distance to $d/L = 0.3$, a different behaviour is observed, characterised by out-of-phase oscillations, which occur after a transient period of $t = 20 - 60$ (see Figure 13b). In this regime, the enclosed fluid between both filaments behaves like a flow generated by a pump due to the out-of-phase flapping, being compressed when the two free ends approach (which is the case of the snapshot displayed in Figure 12b), and released when they move apart. The combined blowing/suction effect produced by the out-of-phase beating of neighbouring filaments resembles the basic mechanism of ciliary propulsion used by small marine invertebrate employing the rhythmic beating of cilia aligned along its body (Dauptain et al., 2008).

Further increasing the spacing to $d/L = 1$, the wake interaction weakens even more and the vortex street behind the filaments is observed to decouple (see Figure 12c). However, beyond 5L downstream of the filaments, the vortices merge into a unique wake and the filaments reach an out-of-phase flapping (see Figure 13c). Upon further increase of the spacing d/L, the two filaments eventually reach an entirely decoupled dynamic.

Finally, the above behaviour is consistent with the experimental observations of Zhang et al. (2000) that report the onset of the out of phase regime at $d/L = 0.21$, compared to our numerical predictions indicating a transitory regime occurring between $d/L = 0.21$ and $d/L = 0.24$.

5. Conclusions

We have described and validated a numerical framework based on the Lattice Boltzmann method coupled to the Immersed Boundary method, able to tackle the fluid-structure interaction of moving bodies, both rigid and flexible. Contrary to previous methods, the solver is entirely free from empirical parameters, and does not require the resolution of any Poisson problem to impose the incompressibility condition by a projection method as is necessary for Navier-Stokes solvers. In particular, the proposed framework enables a precise definition for the numerical thickness of an infinitely thin filament via the ε variable; thereby overcoming the ambiguity highlighted in literature (Eloy et al., 2007; Huang et al., 2007). Moreover we have found that in the case of rigid spherical bodies, the computation of ε can be done out of the temporal loop, keeping a reasonable accuracy and saving considerable CPU time, especially when dealing with multiple moving objects.

The validation cases have demonstrated good agreement for academic configurations involving sharp geometries, particle sedimentation and flapping filaments. In particular, the fluid-structure interaction of flapping filament-like structures is shown to successfully reproduce the wake interactions observed in reference numerical, experimental and physical literature results. The coupled fluid/filament dynamics leading to the various regimes highlighted in §4.3 is found to linked to the effects of rigidity, which reshape the filament in the form of travelling waves, to balance the elastic energy of the filament and the kinetic energy of the fluid.

In the short term, this work will enable ongoing focus on the shape adaptation properties of the flapping filament, within the scope of flow control applications. In particular, slender

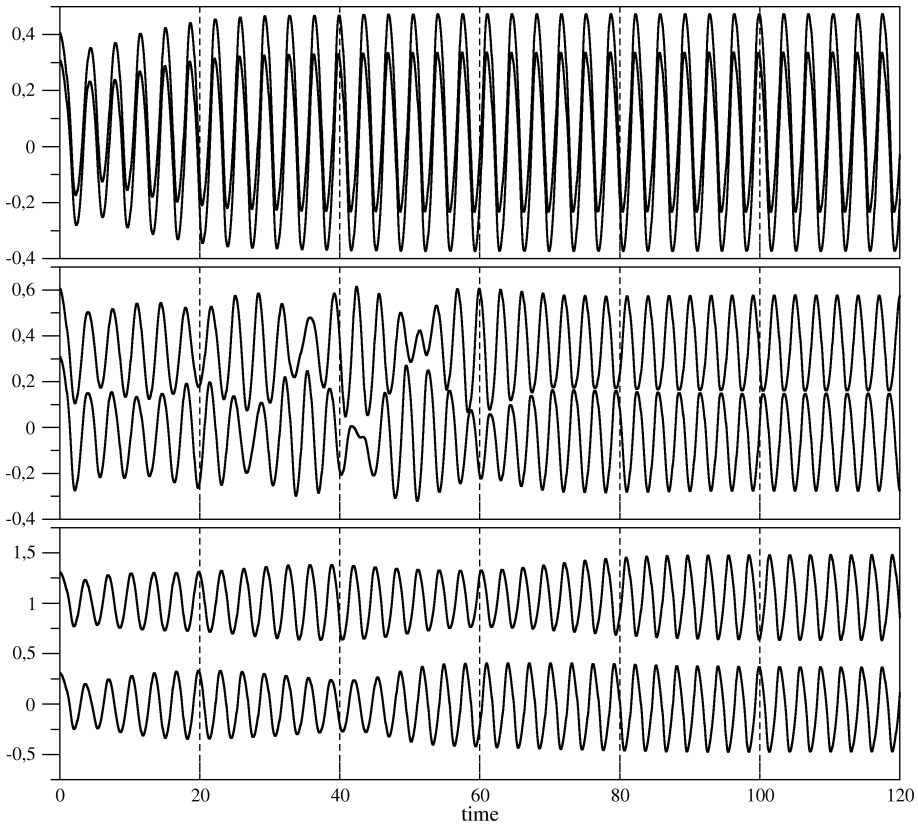

Figure 13: Time evolution of the y-coordinates of the free extremity of a system of two beating filaments using $\rho = 1.5$, $K_B = 0.001$, $Re = 300$ and $Ri = 0.5$. (a) $d/L = 0.1$, (b) $d/L = 0.3$, (c) $d/L = 1.0$.

filament-like structures can be used as a wall coating able to influence the recirculating zones of separated flows (Favier et al., 2009; Bagheri et al., 2012).

Acknowledgements

This work was partially supported by the Spanish Ministry of Economics through the grant DPI2010-20746-C03-02. The authors also acknowledge the financial help of the *PELskin* European project (FP7 AAT.2012.6.3-1). AR thanks Prof. J. Derksen and Dr. A. Kuzmin for starting push at the Workshop in 2011.

References

Aidun, C. K., Ding, E.-J., 2003. Dynamics of particle sedimentation in a vertical channel: period doubling bifurcation and chaotic state. Physiscs of Fluids 15 (6), 1612–1621.

Alben, S., Shelley, M., 2008. Flapping states of a flag in an inviscid fluid: bistability and the transition to chaos. Physical Review Letters 100 (074301).

Bagheri, S., Mazzino, A., Bottaro, A., 2012. Spontaneous symmetry breaking of a hinged flapping filament generates lift. Physical Review Letters 109, 154502.
Bailey, H., 2000. Motion of a hanging chain after the free end is given an initial velocity. American Journal of Physics 68, 764–767.
Bhatnagar, P., Gross, E., Krook, M., 1954. A model for collision processes in gases. i: small amplitude processes in charged and neutral one-component system. Physical Review 94, 511–525.
Chen, S., Doolen, G., 1998. Lattice boltzmann for fluid flows. Annual Review of Fluid Mechanics 30 (1), 329–364.
Dauptain, A., Favier, J., Bottaro, A., 2008. Hydrodynamics of ciliary propulsion. Journal of Fluids and Structures 24 (8), 1156–1165.
Domenichini, F., 2008. On the consistency of the direct forcing method in the fractional step solution of the navier-stokes equations. Journal of Computational Physics 227 (12), 6372–6384.
Eloy, C., Lagrange, R., Souilliez, C., Schouveiler, L., 2008. Aeroelastic instability of cantilevered flexible plates in uniform flow. Journal of Fluid Mechanics 611, 97–106.
Eloy, C., Souilliez, C., Schouveiler, L., 2007. Flutter of a rectangular plate. Journal of Fluids and Structures 23 (6), 904–919.
Fadlun, E., Verzicco, R., Orlandi, P., Mohd-Yusof, J., 2000. Combined immersed-boundary finite-difference methods for three–dimensional complex flow simulations. Journal of Computational Physics 161, 35–60.
Favier, J., Dauptain, A., Basso, D., Bottaro, A., 2009. Passive separation control using a self-adaptive hairy coating. Journal of Fluid Mechanics 627, 451.
Feng, Z., Michaelides, E., 2004. The immersed boundary-lattice boltzmann method for solving fluidparticles interaction problems. Journal of Computational Physics 195 (2), 602–628.
Glowinski, R., Pan, T. W., Hesla, T. I., Joseph, D. D., Périaux, J., 2001. A fictitious domain approach to the direct numerical simulation of incompressible viscous flow past moving rigid bodies: Application to particulate flow. Journal of Computational Physics 169 (2), 363–426.
Guo, Z., Zheng, C., Shi, B., 2002. Discrete lattice effects on the forcing term in the lattice boltzmann method. Phys. Rev. E 65, 046308.
He, X., Luo, L., 1997. A priori derivation of the lattice boltzmann equation. Physical Review E 55 (6).
Huang, W.-X., Shin, S. J., Sung, H. J., 2007. Simulation of flexible filaments in a uniform flow by the immersed boundary method. Journal of Computational Physics 226 (2), 2206 – 2228.
Ikeno, T., Kajishima, T., 2007. Finite-difference immersed boundary method consistent with wall conditions for incompressible turbulent flow simulations. Journal of Computational Physics 226 (2), 1485–1508.
Koumoutsakos, P., Shiels, D., 1996. Simulations of the viscous flow normal to an impulsively started and uniformly accelerated flat plate. Journal of Fluid Mechanics 328, 177–227.
Malaspinas, O., Sagaut, P., 2012. Consistent subgrid scale modelling for lattice boltzmann methods. Journal of Fluid Mechanics 700 (1), 514–542.
Marié, S., Ricot, D., Sagaut, P., 2009. Comparison between lattice boltzmann method and navier–stokes high order schemes for computational aeroacoustics. Journal of Computational Physics 228 (4), 1056–1070.
Mittal, R., Dong, H., Bozkurttas, M., Najjar, F., Vargas, A., Loebbecke, A. V., 2008. A versatile sharp interface immersed boundary method for incompressible flows with complex boundaries. Journal of Computational Physics 227 (10), 4825–4852.
Païdoussis, M. P., 2004. Fluid-structure interactions: slender structures and axial flow, volume 2. Elsevier Academic Press.
Peskin, C. S., 2002. The immersed boundary method. Acta Numerica 11, 479–517.
Pinelli, A., Naqavi, I., Piomelli, U., Favier, J., 2010. Immersed-boundary methods for general finite-difference and finite-volume navier-stokes solvers. Journal of Computational Physics 229 (24), 9073 – 9091.
Qian, Y., DHumieres, D., Lallemand, P., 1992. Lattice bgk models for navier–stokes equation. Europhysics Letters 17 (6), 479–484.
Rayleigh, L., 1878. On the instability of jets. Proceedings of the London mathematical society 10, 4–13.
Roma, A. M., Peskin, C. S., Berger, M. J., 1999. An adaptive version of the immersed boundary method. Journal of Computational Physics 153, 509 – 534.
Shan, X., Yuan, X.-F., Chen, H., 2006. Kinetic theory representation of hydrodynamics: a way beyond the navierstokes equation. Journal of Fluid Mechanics 550 (1), 413–441.
Shelley, M. J., Zhang, J., 2011. Flapping and bending bodies interacting with fluid flows. Annual Review of Fluid Mechanics 43 (1), 449–465.
Succi, S., 2001. The lattice Boltzmann equation. Oxford university press New York.
Taira, K., Colonius, T., 2007. The immersed boundary method: A projection approach. Journal of Computational Physics 225 (10), 2118–2137.
Tian, F.-B., Luo, H., Zhu, L., Liao, J. C., Lu, X.-Y., 2011. An efficient immersed boundary-lattice Boltzmann method for the hydrodynamic interaction of elastic filaments. Journal of Computational Physics.

Uhlmann, M., 2005. An immersed boundary method with direct forcing for the simulation of particulate flows. Journal of Computational Physics 209 (2), 448–476.

Wu, J., Shu, C., 2009. Implicit velocity correction-based immersed boundary-lattice Boltzmann method and its applications. Journal of Computational Physics 228 (6), 1963–1979.

Wu, J., Shu, C., 2010. An improved immersed boundary-lattice Boltzmann method for simulating three-dimensional incompressible flows. Journal of Computational Physics 229 (13), 5022–5042.

Zhang, J., Childress, S., Libchaber, A., Shelley, M., 2000. Flexible filaments in a flowing soap film as a model for one-dimensional flags in a two-dimensional wind. Nature 408, 835–839.

Zhu, L., Peskin, C. S., 2000. Interaction of two flapping filaments in a flowing soap film. Physics of fluids 15, 1954–1960.

Zhu, L., Peskin, C. S., 2002. Simulation of a flapping flexible filament in a flowing soap film by the immersed boundary method. Physics of fluids 179, 452–468.